



# Enhanced contrast imaging with polyamide 6/Fe(OH)<sub>3</sub> nanofibrous scaffolds: A focus on high T<sub>1</sub> relaxivity

Congyi Yang<sup>a</sup>, Yifan Jia<sup>a</sup>, Weiwen Yuan<sup>b</sup>, Guoxing Liao<sup>a</sup>, Qianqian Yu<sup>a,\*</sup>, Zhe Tang<sup>a</sup>, Yuan Ji<sup>a</sup>, Guanghui Liu<sup>a</sup>, Fangrong Tan<sup>a</sup>, Paul D. Topham<sup>c,\*</sup>, LinGe Wang<sup>a,\*</sup>

<sup>a</sup> South China Advanced Institute for Soft Matter Science and Technology, School of Emergent Soft Matter, Guangdong Provincial Key Laboratory of Functional and Intelligent Hybrid Materials and Devices, Guangdong Basic Research Center of Excellence for Energy & Information Polymer Materials, State Key Laboratory of Luminescent Materials and Devices, South China University of Technology, Guangzhou 510640, China

<sup>b</sup> Guangdong Second Provincial General Hospital, Guangzhou 510317, China

<sup>c</sup> Chemical Engineering and Applied Chemistry, School of Infrastructure and Sustainable Engineering, College of Engineering and Physical Sciences, Aston University, Birmingham B4 7ET, United Kingdom

**Keywords:** Electrospinning, Magnetic nanofibers, Magnetic resonance imaging, T<sub>1</sub> positive contrast, Iron-based scaffolds, Polyamide 6

Nanofibers serve as widely employed tissue engineering scaffolds in diverse biomedical applications. When implanted *in vivo*, it is crucial for tissue engineering scaffolds to be visualizable, enabling the monitoring of their shape, position, and performance. This capability facilitates the effective assessment of implant deformations, displacements, degradations, and functionalities. However, in many biomedical imaging techniques such as magnetic resonance imaging (MRI), the contrast of tissue engineering scaffolds is often inadequate. MRI is particularly notable for its effectiveness in imaging soft tissues. Previous endeavors to enhance the contrast of tissue engineering scaffolds in MRI have involved the use of negative contrast agents (CAs). Nonetheless, negative CAs can result in artifacts, thus favoring the preference for positive CAs due to their ability to generate clearer boundaries. In this study, we successfully prepared composite polyamide 6 nanofibrous scaffolds with ultrafine dispersion Fe(OH)<sub>3</sub> nanoparticles using electrospinning and *in-situ* growth techniques. The relaxation properties of the magnetic nanofibrous scaffolds confirmed the successful production of scaffolds suitable for positive imaging. *In vitro* cell seeding experiments demonstrated the efficient proliferation and adhesion of endothelial cells and fibroblasts. *In vivo* studies further revealed the biocompatibility and functionality of the scaffolds. These findings indicate that the prepared PA6/Fe(OH)<sub>3</sub> composite nanofibrous scaffolds can enable straightforward, safe, and efficient *in vivo* positive contrast MRI monitoring, thereby playing a pivotal role in the integration of diagnosis and treatment within tissue engineering scaffolds.

\* Corresponding authors.

E-mail addresses: [yuqianqian@scut.edu.cn](mailto:yuqianqian@scut.edu.cn) (Q. Yu), [p.d.topham@aston.ac.uk](mailto:p.d.topham@aston.ac.uk) (P.D. Topham), [lingewang@scut.edu.cn](mailto:lingewang@scut.edu.cn) (L. Wang).

Received 26 January 2024; Received in revised form 23 March 2024; Accepted 26 March 2024

## 1 Introduction

Tissue engineering is dedicated to the repair of damaged tissues and organs *in vivo* by using scaffolds with or without attached cells [1], including bone [2], vascular scaffolds [3] and neural tissue engineering scaffolds [4]. Such extracellular matrix-like tissue engineering scaffolds are well-designed with porous [5], fibrous [6], and network [7] structures to provide mechanical and structural supports and promote cell-scaffold interactions. However, the progress of clinic translation of tissue engineering scaffolds has been hindered by difficulties associated with monitoring the scaffold in terms of location, function, maturation, acceptance and remodeling after implantation [8].

To monitor implantable materials, commonly used imaging modalities include X-ray [9,10], computerized tomography (CT) [11], magnetic resonance imaging (MRI) [12,13] and ultrasound [14]. X-ray and CT imaging expose tissues to ionizing radiation, while ultrasound has limited tissue penetration. MRI, on the other hand, is a non-ionizing radiation imaging modality that has the advantage of high contrast for soft tissue imaging and is of wide interest for implant imaging [15]. Magnetic nanoparticles (MNPs), as a particularly promising candidate for the contrast media, have received significant attention in the field of MRI contrast agents (CAs) due to their unique nanoscale physicochemical properties and broad application potential [16,17].

The visualization methods of scaffolds are divided into two types of modalities: direct visualization and indirect visualization [8]. For indirect visualization, MNPs are incorporated into cells that have been embedded into scaffolds. For example, Perea *et al.* used clinically approved superparamagnetic nanoparticles to label human umbilical vein endothelial cells (HUVEC), which were then delivered onto polytetrafluoroethylene tubular grafts [18]. Constantinides *et al.* [19] used perfluorocrown-ether-nanoparticles to label murine cardiac progenitor cells and seed them onto porous film scaffolds. For direct visualization, MNPs are incorporated into the scaffolds themselves [20]. These MNPs have been manganese-based [21], gadolinium-based [12] or iron-based [8]. Both methods have been shown to be viable and accurate in identifying implants, however, direct visualization is simpler in terms of fabrication and can be applied to some non-cellularized implants. The MNP CAs are divided into two types: a negative CA that darkens the image and a positive CA that brightens the image [22]. In clinical diagnosis, positive contrast enhancement is favored due to the creation of sharper edges and exhibits no magnetic susceptibility-related artifacts, which can hamper the image quality [22,23]. The ratio of “relaxivities” ( $r_2/r_1$ ) determines whether the CA is positive or negative. Conventionally, CAs with  $r_2/r_1 < 5$  are termed as  $T_1$  CAs, while those having ratio with  $r_2/r_1 > 5$  are termed as  $T_2$  agents [24]. In general, for MNP imaging systems, the particle size, shape, surface state, and crystal structure all have an impact on the relaxation rate. A small particle size contributes to  $T_1$ -weighted imaging [16]. For example, iron-based CAs with positive contrast function have been successfully developed by reducing the size of nanoparticles [25–27]. A study by Liu *et al.* discovered that the  $r_2/r_1$  values of 3-(3,4-dihydroxyphenyl) propionic acid (DHCA)-modified  $Fe_3O_4$  nanoparticles were 1.99, 3.1 and 4.05 (at 0.5 T) for NPs with

diameters of 4, 8, 12 nm, respectively [26]. In other related work, Peng and co-workers compared the  $r_2/r_1$  values of iron oxide hydroxide (FeOOH) nanoparticles (< 4 nm diameter,  $r_2/r_1 \sim 3$  at 0.47 T) with those of FeOOH nanoclusters (approximately 40 nm in diameter,  $r_2/r_1 \sim 26$  at 0.47 T) [25]. Besides reducing the size of the nanoparticles, other means to reduce  $r_2/r_1$  include suppressing magnetization effects, such as through the use of antiferromagnetic FeOOH nanoparticles [28]. Other examples of iron-based positive CAs include FeOOH nanospindles ( $r_2/r_1 = 1.65$  at 1.5 T) [29] and iron oxide nanowhiskers ( $r_2/r_1 = 1.83$  at 1.4 T) [30].

The inherent problem with positive contrast iron-based scaffolds is how to achieve smaller CA particle size within the scaffolds. Preparing scaffolds containing iron oxide through physical blending is a facile fabrication method. However, the iron-based scaffolds prepared by this method mostly achieve negative contrast enhancement, primarily due to the agglomeration and large particle size of the MNPs within the polymer matrix [20,31–33]. Recently, Marc-André Fortin’s team successfully prepared an alginate-based hydrogel with positive contrast effect using PEG-stabilized ultra-small iron oxide nanoparticles (USIONPs) with an average diameter of 4.9 nm [22]. However, these PEG-stabilized USIONPs underwent thermal decomposition and ligand exchange, which was excessively complex. Therefore, we need to choose a preparation method that is simple and allows for the uniform dispersion of MNPs in the polymer matrix. It was reported that *in situ* fabrication could enable uniform dispersion of MNPs in polymer matrices [33,34]. Nanofibers have an extremely high specific surface area, which can provide a larger loading area and more attachment sites for the growth of MNPs, thereby facilitating the highly uniform dispersion of MNPs [35].

Electrospinning is a simple method for preparing continuous nanofibers of various polymers, polymer blends and polymers/inorganic particles composites, and useful in a variety of applications such as tissue engineering, drug delivery, and filtration [36–42]. Recently, ligand stabilization methods have been widely used to enhance the dispersion of metals and improve the stability of metal sites [43]. In our previous work and the work of the aforementioned researchers, we have found that the fractional state of CAs has a significant impact on MRI performance. We have already verified this in an electrospun poly(ethylene terephthalate)/gadolinium hydroxide nanofibrous system [12]. However, we need a broader understanding of whether the concept that good dispersion leads to good MRI performance is generally applicable. Therefore, herein, we aimed to achieve our objective by the *in situ* synthesis of  $Fe(OH)_3$  particles within polyamide 6 (PA6) nanofibers. PA6 is an FDA-approved implant material with the ability to coordinate with iron ions. Its structural similarity to bone collagen makes it a promising choice for tissue engineering and biomedical applications [44,45]. Therefore, in this study, PA6 was chosen as the fibrous (supporting) matrix. After successful fabrication of the PA6/ $Fe(OH)_3$  composite nanofibrous scaffolds, we assessed their relaxivity, biocompatibility, cell adhesion, and *in vivo* MRI imaging capability. Furthermore, we conducted *in vivo* MRI experiments using scaffolds with three different concentrations

of iron hydroxide to further evaluate the feasibility for biomedical applications. This study successfully achieved direct labeling of scaffolds with CAs. The combined *in situ* imaging, along with non-invasive monitoring, can provide comprehensive information on tissue repair, laying the foundation for constructing intelligent tissue engineering scaffolds.

## 2 Experimental section

### 2.1 Materials

Ferric chloride ( $\text{FeCl}_3$ , 98%, Switzerland) was purchased from Adams, soda lime ( $\text{NaOH}$ , 98%, Switzerland), formic acid (FA, General-Reagent,  $\geq 98\%$ ), PA6 granules (YH800, Hunan Yuehua chemical Co. Ltd, China), phosphate buffered saline (PBS) buffer (PH = 7.4, Gibco), fetal bovine serum (FBS, sterile, Gibco), Dulbecco's modified eagle medium (DMEM basic 1  $\times$ , Gibco), and antibiotics (penicillin-streptomycin 10000  $\mu\text{mL}^{-1}$ ) were purchased from Beyotime Biotechnology (Nantong, China). All chemicals were used without further purification. Penicillin-streptomycin solution (100  $\times$ ), trypsin cell digest (0.25% trypsin, containing phenol red), immunostaining permeabilization buffer with triton X-100, 4% paraformaldehyde fix solution, cell counting kit-8 (CCK-8), actin-tracker green-488 and DAPI staining solution were purchased from Beyotime Biotechnology (Nantong, China). Anticoagulant rabbit blood with sodium citrate was purchased from HongQuan Bio company (Guangzhou, China). Hematoxylin-Eosin (H&E) was purchased from Servicebio (Wuhan, China). Deionized water was obtained from an Elga DV25 water purifier unit.

### 2.2 Animals

SD rats (5 - 6 weeks old females with average weights of 180 - 210 g) were purchased from Hunan Slac laboratory animal Co. Ltd (Changsha, China). The care and use of animals were performed in compliance with guidelines of the Regional Ethics Committee for Animal Experiments, and were approved by the Institutional Animal Care and Use Committee of SCUT (AEC No. 2020048).

### 2.3 Preparation of PA6/Fe(OH)<sub>3</sub> nanofibrous scaffold

A handmade uniaxial electrospinning machine was used to manufacture the nanofibrous scaffold [46]. The fabrication procedure of nanofibers is shown in Figure 1. PA6 nanofibers solutions were prepared with varied iron concentration, in which the weight ratio of iron and PA6 was 0.1, 0.2, 0.4, 0.7, 1, 2, 4, 7 wt%:1 wt%, respectively. In a typical fabrication procedure, 0.2  $\text{g}\cdot\text{mL}^{-1}$   $\text{FeCl}_3\cdot 6\text{H}_2\text{O}$ /FA solution was prepared. 3 g of PA6 were mixed with 6.94 mL FA and dissolved at room temperature under magnetic stirring for 16 h. Then, 0.0724 mL of  $\text{FeCl}_3\cdot 6\text{H}_2\text{O}$ /FA solution (Fe: PA6 = 0.1 wt%:1 wt%) were added into the transparent PA6/FA solution, followed by magnetic stirring for 8 h. Before electrospinning, ultrasonication was applied to help the dispersion of  $\text{FeCl}_3\cdot 6\text{H}_2\text{O}$  in the solution. Each of the mixed solutions was placed into a 10 mL syringe equipped with a stainless steel needle (21 gauge). The needle was connected to a high voltage power supply with 30 kV positive voltage (TL-pro, Tongli tech), and the collector was a grounded drum with 15 cm diameter at the rotational speed of 30 rpm. For all samples, the distance between the needle tip and the drum was kept at 10 cm,

the flow rate maintained at 0.3  $\text{mL}\cdot\text{h}^{-1}$ , temperature held at 24 - 27°C, and the humidity controlled between 40 - 55% relative humidity (RH) to prevent electrical leakage. All obtained fibers were then dried in a vacuum oven for 24 h at room temperature to remove residual solvent. The as-spun  $\text{FeCl}_3$ /PA6 nanofibrous scaffold was immersed in 250 mL  $\text{NaOH}$  (pH = 12) aqueous solution overnight to convert  $\text{FeCl}_3$  to  $\text{Fe(OH)}_3$ . The nanofibrous scaffold were washed with deionized water until the drained water achieved neutral pH. Then, the nanofibrous scaffold was dried in a 40°C blowing oven for 72 h and stored in a dry box for further use. The PA6/Fe(OH)<sub>3</sub> 0.1 wt% nanofibrous scaffold are denoted by 0.1PA6 scaffold throughout this manuscript, with the other groups abbreviated in the same fashion.

### 2.4 Characterization

#### 2.4.1 Characterization of electrospun PA6/Fe(OH)<sub>3</sub> nanofibrous scaffold

**2.4.1.1 Scanning electron microscopy (SEM).** The morphology of the PA6/Fe(OH)<sub>3</sub> nanofibrous scaffold was characterized by SEM (JSM-7900F, JEOL, Japan) with an acceleration voltage set at 5 kV. The nanofibrous scaffold was cut into 5  $\times$  5 mm<sup>2</sup> pieces fixed on SEM stubs and sputtered with Pt for 60 s by an ion sputter (Q150T ES PLUS, Quorum, U.K.). Observations were conducted in the magnification range of 1500  $\times$  to 7000  $\times$  with a working distance of 10 mm. Fiber diameters were measured by ImageJ software (~100 nanofibers counted per sample). Energy-dispersive X-ray spectroscopy (EDS) analysis of C, H, O, N, Fe was employed with an integration time of 90 seconds for the detector, collected in the energy range of approximately 12 keV. Taking into account the detection sensitivity of EDS mapping, aiming to achieve improved signal intensity, contrast, and reduced noise, 7PA6 scaffold was selected for mapping analysis.

**2.4.1.2 Transmission electron microscopy (TEM).** The distribution of Fe(OH)<sub>3</sub> NPs throughout the nanofibrous scaffold was observed by TEM (JEM-1400 Flash, JEOL, Japan), operating at 120 kV. Fibers were directly spun on a copper grid for characterization using TEM and EDS under high-angle annular dark field (HAADF). The sample fabrication process involved electrospinning the nanofibers onto the copper grid and  $\text{NaOH}$  (pH = 12) solution treatment of the nanofibers (to convert  $\text{FeCl}_3$  to  $\text{Fe(OH)}_3$ ) and thrice immersion in DI water. The chemical composition and iron distribution of nanofibrous scaffold was characterized by energy dispersive spectroscopy (EDS) and HAADF with JEM-2100F (JEOL, Japan). Considering the marginal differences observed in the TEM images for the morphology of Fe(OH)<sub>3</sub> NPs of 2PA6 - 7PA6 scaffolds, further characterization of Fe(OH)<sub>3</sub> species was conducted using high resolution transmission electron microscopy (HRTEM), EDS and selected area electron diffraction (SAED) techniques on 7PA6 scaffold.

**2.4.1.3 X-ray diffraction (XRD).** The crystalline structure was analyzed by XRD (X'pert Powder, PANalytical, Netherlands) with copper target ( $\lambda = 1.5406 \text{ \AA}$ ), scanning from 10° to 40° at 12°·min<sup>-1</sup>.



Fig. 1

Schematic illustration of the preparation process of PA6/Fe(OH)<sub>3</sub> nanofibrous scaffold. PA6 nanofibers with varied iron concentration is achieved through FeCl<sub>3</sub>·6H<sub>2</sub>O/FA solution preparation, magnetic stirring, and ultrasonication for improved dispersion. Subsequent electrospinning (to create nanofibers) and alkali treatment (to convert FeCl<sub>3</sub> to Fe(OH)<sub>3</sub>) produced PA6/Fe(OH)<sub>3</sub> nanofibrous scaffold with varied iron content.

**2.4.1.4 Fourier-transform infrared spectroscopy (FTIR).** The chemical functional groups of the nanofibrous scaffolds were observed by FTIR (Bruker VERTEX 70, Bruker, Germany) using 1 × 1 cm samples cut from the original fabric. FTIR measurements were performed in attenuated total reflection (ATR) mode and spectra were collected in the range of 4000 - 600 cm<sup>-1</sup> with a signal resolution of 1 cm<sup>-1</sup>. Each spectrum was an average of 64 scans to improve the signal-to-noise ratio.

**2.4.1.5 X-ray photoelectron spectroscopy (XPS).** The chemical composition of the surfaces of the nanofibrous scaffolds were obtained by XPS (EscaLab XI+, Thermo Scientific, USA) using monochromatic Al K $\alpha$  X-rays ( $h\nu = 1486.6$  eV) with a spot size of 500  $\mu$ m and depth of 10 nm. Survey spectra were acquired in the energy range of 0 - 1350 eV, while high-resolution spectra were collected for C, N, O and Fe. Taking into consideration the depth detection limitations, 0, 0.7, 1 and 7PA6 scaffolds were selected for analysis based on the concentration of iron when Fe(OH)<sub>3</sub> aggregates appeared in the TEM images.

**2.4.1.6 Physical property measurement system (PPMS).** Magnetic properties were recorded by a vibrating sample magnetometer (VSM) in the PPMS (PPMS&Evercool, Qyantum Design Inc., USA) at 298 K with  $\pm 10$  kOe applied field.

**2.4.1.7 Thermogravimetric analysis (TGA).** TGA (STA449 F3, NETZSCH, Germany) was conducted under a nitrogen atmosphere to investigate thermal stability and decomposition behavior using a heating rate of 10°C/min. Samples weighing in the range of 5 - 10 mg were loaded onto a platinum crucible. The temperature range for the analysis was set from 30°C to 800°C to cover the expected decomposition or degradation temperature range.

**2.4.1.8 Mechanical stretching test.** Tensile tests (LD22.102, ShenZhen Lanbosansi Material Testing Co., Ltd, China) were conducted at a stretching rate of 5 mm·s<sup>-1</sup>. All samples were cut into rectangles with 80 mm length and 20 mm width. The tensile test was carried out until the sample fractured, and the load and displacement data were continuously recorded during the test.

Stress-strain curves were obtained by dividing the applied load by the original cross-sectional area of the sample. The ultimate tensile strength, Young's modulus and elongation at break were determined from the stress-strain curves. Experiments were performed in triplicate at ambient temperature.

**2.4.1.9 Inductively coupled plasma-optical emission spectroscopy (ICP-OES).** The actual iron content in the nanofibrous scaffolds were determined using ICP-OES. Samples were digested using 10% (v/v) HNO<sub>3</sub> to extract the iron. The digested solutions were then analyzed using ICP-OES to quantify the iron content and mass fraction. Based on the results of *in vitro* MRI tests, we observed that 0.7PA6 scaffold exhibited the strongest positive contrast signal, while 7PA6 scaffold displayed the strongest negative contrast signal. Therefore, 0.2PA6, 0.7PA6, 2PA6 and 7PA6 were selected for evaluation the *in vitro* release rate of Fe.

Iron release tests (Optima 8300, PE, America) of nanofibrous scaffolds were conducted with the following steps: 10 mg nanofibrous scaffolds were immersed in 10 mL PBS buffer (pH=7.4) at 37°C on the shaker throughout the experimental period and 2 mL soaking solution was taken at each time point to detect the Fe content by ICP-OES. 2 mL of fresh PBS buffer were added into the original nanofibrous scaffold immersion after each withdrawal. The Fe content of pure PBS buffer was also detected and used as background deduction. The same step was repeated after changing the release solution as PBS buffer.

**2.4.1.10 Relaxivity measurements.** The  $r_1$  and  $r_2$  relaxation times were measured by MQ20 (Brooke, Germany) at 40°C, 0.5 T. Samples were placed in the low field nuclear magnetic resonance (LFNMR) tube in an infiltrated state with ultrapure water.  $r_1$  relaxation times were determined using an inversion recovery pulse sequence (IR) sequence, with a recycle delay of 20 s, scan of 4 times, gain of 53 dB, first separation = 0.5 ms, final separation = 4000 ms and fitting number of points = 10.  $r_2$  relaxation times were determined using a Carr Purcell Meiboom Gill (CPMG) sequence, with a recycle delay of 20 s, scan of 8 times, gain of 56 dB.

**2.4.1.11 In vitro MR imaging.** MRI was operated on a 3.0 T system (Philips, Netherlands). The samples soaked with ultrapure water were placed in flat-bottomed glass bottles and then placed in a head coil. Sequence parameters: T<sub>1</sub>-weighted imaging (T<sub>1</sub>WI, which utilizes the longitudinal relaxation properties of protons to generate contrast and depict variations in their T<sub>1</sub> relaxation times) inverse recovery, TE = 20 ms, TR = 2045 ms, TI = 800 ms, and 0.65 mm × 0.81 mm voxel with 4 mm slice thickness; T<sub>2</sub>-weighted imaging (T<sub>2</sub>WI, which utilizes the transverse relaxation properties of protons to generate contrast and depict variations in their T<sub>2</sub> relaxation times) turbo spin echo (TSE), TE = 105 ms, TR = 3000 ms, TSEes/shot = 7.8/171 ms and 0.3 mm × 0.3 mm voxel with 1 mm slice thickness. The signal intensity values within the region of interest (ROI) were analyzed using MicroDicom viewer for statistical analysis of the acquired images. The software also provided error analysis for the data.

## 2.4.2 Cellular experiments

**2.4.2.1 Cell culture.** Mice embryonic fibroblast cells (NIH/3T3) and HUVEC were cultured in DMEM with 10 wt% FBS and 1% antibiotics and incubated at 37°C, 5% CO<sub>2</sub> and 95% RH.

**2.4.2.2 Cell counting kit-8 (CCK-8) assay.** CCK8 assays were conducted with both NIH/3T3 cells and HUVEC according to ISO 10993-12:200 [47]. In brief, nanofibrous scaffolds were incubated in DMEM for 24 h at 37 °C and the extracts were performed in cell culture. For the experimental group, 20 μL of the NIH/3T3 cells or HUVEC suspension (with a density of 5 × 10<sup>4</sup> mL<sup>-1</sup>) and 180 μL extracts were used in each well of the 96-well plate for 24 h incubation. For the control group, 180 μL DMEM was used instead of extracts. For the blank group, the culture medium containing 20 μL of sterile PBS buffer (pH = 7.4) and 180 μL DMEM was used. After 24 h cell incubation, 20 μL of CCK-8 solution were added and incubated for 4 h and the optical density (OD) value at 450 nm was examined by microplate reader (SpectraMax iD3, Molecular Devices, USA). The cell viability was calculated by Eq. 1, where OD sample denotes the OD value of sample group, OD blank denotes the OD value of cultivation medium, and OD control denotes the OD value of control group:

$$\text{Cell viability (\%)} = \frac{(\text{OD}_{\text{sample}} - \text{OD}_{\text{blank}})}{(\text{OD}_{\text{control}} - \text{OD}_{\text{blank}})} \times 100\% \quad (1)$$

**2.4.2.3 In vitro hemolysis assay.** To evaluate the extent of hemolysis *in vitro*, a hemolysis test was conducted using rabbit blood as the test sample. Briefly, rabbit red blood cells (RBCs) were purified by centrifugation at 1500 rpm and washed three times with PBS (pH = 7.4), then the rabbit RBCs were suspended in 5 mL of PBS (pH = 7.4). Subsequently, after adding the diluted blood into each centrifuge tube, a fibrous scaffold sample was placed in each tube. The tubes were then incubated in a stationary mode for 4 hours at 37 °C. Simultaneously, the same volume of diluted blood was added into PBS (pH = 7.4) or deionized water for negative and positive controls, respectively. After incubation, all samples were centrifuged at 1500 rpm for 5 minutes. Finally, the OD value of the supernatant at 540 nm [48] was determined and the hemolysis rate was calculated by the Eq 2 (where OD<sub>sample</sub>

denotes the OD value of the sample group, OD<sub>negative</sub> denotes the OD value of the red cells incubated with PBS, and OD<sub>positive</sub> denotes the OD value of the red cells incubated with H<sub>2</sub>O):

$$\text{Hemolysis rate (\%)} = \frac{(\text{OD}_{\text{sample}} - \text{OD}_{\text{negative}})}{(\text{OD}_{\text{positive}} - \text{OD}_{\text{negative}})} \times 100\% \quad (2)$$

**2.4.2.4 Cell colonization, staining and microscopy.** The nanofibrous scaffolds with flat surface were placed in a 24-well plate before HUVEC and NIH/3T3 cells were seeded on the scaffolds at a concentration of 2500 cells·μL<sup>-1</sup> and cultured for 48 h. Afterwards, the scaffolds were washed with PBS, fixed with paraformaldehyde solution for 15 min, permeabilized by a 0.1% (v/v) Triton-X-100 PBS solution and the cytoskeleton was stained by phalloidin-fluorescein isothiocyanate (FITC) and cell nucleus stained with DAPI. The cells colonizing on the scaffold were observed by confocal laser scanning microscopy (CLSM).

## 2.5 In vivo experiment

A total of 15 female SD rats were used. Each rat underwent a surgical procedure with subcutaneous implantation of a cylindrical sample of 2 mm diameter and 1.5 cm length at a 3 mm depth into the left-back sites. MRI investigation was carried out on day 1, 2, 3, 5, 8 post-implantation. At the time of sacrifice, heart, liver, spleen, lungs and kidneys were harvested and fixed, dehydrated, embedded, sectioned and hematoxylin/eosin (H&E) stained for optical microscopy observations. A rat with surgical operation but without implantation was harvested as a control (or 'sham') group. Based on the results obtained from *in vitro* MRI, OPA6, 0.7PA6, and 7PA6 scaffolds were selected for *in vivo* MRI analysis.

## 2.6 Statistical analysis

Statistical analysis was employed to compare different groups using the Student's t-test. The data were represented as mean ± standard deviation. Results with \* p < 0.05, \*\* p < 0.01, and \*\*\* p < 0.001 were considered statistically significant, while non-significant differences were indicated as not significant (n.s.).

## 3 Results and discussion

### 3.1 Preparation and structural characterization of PA6/Fe(OH)<sub>3</sub> nanofibrous scaffold

The aim of this study was to fabricate positive contrast scaffolds using iron-based CAs. Different concentrations of FeCl<sub>3</sub>, with Fe: PA6 ranging from 0.1 wt% to 7 wt%, were added to PA6 electrospinning solutions (before being converted to Fe(OH)<sub>3</sub> by a post-electrospinning alkali treatment) were employed to determine the optimal concentration for the positive contrast. A concentration-dependent deepening of color of the FeCl<sub>3</sub>/PA6 nanofibrous scaffold was observed (Figure S1). The actual content of Fe in each PA6/Fe(OH)<sub>3</sub> nanofibrous scaffold was determined by ICP-OES, as shown in Table S1. The actual content did not differ significantly from the expected content when the Fe content was lower than 1 wt% (error ranging of 4% - 20%). However, it was also found that the loss of Fe from the scaffold after alkali treatment was higher when the Fe content in the spinning solution was

higher, especially for 7PA6 scaffold, where the actual content of Fe in the final nanofibrous scaffold was only 4.11 wt.%.

To confirm the formation of  $\text{Fe}(\text{OH})_3$  after NaOH treatment, analysis was conducted using SEM and XPS. SEM studies of OPA6 - 7PA6 scaffold proved that fibrous morphologies of OPA6 - 7PA6 scaffold did not change after soaking in NaOH solution. The average diameter of fibers with increased iron contents, ranged from  $\sim 250$  nm for OPA6 scaffold to  $\sim 1670$  nm for 7PA6 scaffold. Surface morphology of the fibers with iron content lower than 0.93 wt% (OPA6 - 1PA6 scaffolds) were smooth. When the Fe concentration continued was increased, fibers became wrinkled and coarse (2PA6 - 7PA6 scaffolds) (Fig. 2a). EDS mapping of 7PA6 scaffold indicates uniform distribution of Fe throughout the PA6 matrix (Fig. 2b). C, N, O elements were attributed to PA6. Besides, a trace amount of Cl was also detected (0.12 wt%). Comparing the EDS mapping results of 7% $\text{FeCl}_3/\text{PA6}$  with  $\text{PA6}/\text{Fe}(\text{OH})_3$  7% scaffold, it was observed that the ratio of iron to chlorine content increased from 1.4:1 (Figure S2 b1) to 30.7:1 (Figure S2b2), indicating almost complete conversion of  $\text{FeCl}_3$ . The full scan XPS spectrum showed the existence of C, N, O and Fe elements (Fig. 2c1). The peaks around 978 eV and 998 eV are attributed to Auger peaks of O, while the peak around 1104 eV is attributed to Auger peaks of N, and the peak around 1226 eV is attributed to Auger peak of C. The O 1s displayed at 531.4 eV of OPA6 and 0.7PA6 scaffolds were attributed to the C=O in PA6, whereas the O 1s peak of Fe-O was not seen in 0.7PA6, which could be due to the low content of iron on the surface (Fig. 2c3). Fe-O peaks at 528.3 eV and 529.1 eV were observed for 1PA6 and 7PA6, respectively [49]. The state of the iron in  $\text{PA6}/\text{Fe}(\text{OH})_3$  nanofibrous scaffold was determined by XPS. As shown in Figure S1c, the peaks of Fe  $2p_{1/2}$  and Fe  $2p_{3/2}$  centered at 724.6 and 710.9 eV. The satellite peaks at around 718 and 732 eV evidenced that no  $\text{Fe}^{2+}$  species existed [25].

To investigate the aggregation and dispersion of  $\text{Fe}(\text{OH})_3$  in PA6 scaffold, TEM, EDS and SAED were employed for characterization. The results indicate that aggregation of  $\text{Fe}(\text{OH})_3$  in the PA6 scaffold was only observed when the iron content exceeds 1%. This implies that at iron contents below 1wt%,  $\text{Fe}(\text{OH})_3$  exhibits good dispersion in the PA6 fiber without significant aggregation. As the iron content increases, the  $\text{Fe}(\text{OH})_3$  NPs may start to aggregate and form clusters or agglomerates (Fig. 3a). The EDS results confirm that the aggregates on the surface of the PA6 fiber consist of iron and oxygen, further supporting their composition as  $\text{Fe}(\text{OH})_3$  (Fig. 3b). No distinct crystal areas were observed in the  $\text{Fe}(\text{OH})_3$  grains and the SAED patterns show no diffraction spots, indicating that  $\text{Fe}(\text{OH})_3$  is amorphous in nature (Fig. 3c1,c2,c3). Due to the amorphous nature of the  $\text{Fe}(\text{OH})_3$  observed in the scaffold through HRTEM and SAED, its crystalline structure was further probed using XRD. The XRD results are shown in Figure S3. The diffraction peaks at  $11^\circ$ ,  $20.3^\circ$ ,  $21.4^\circ$  and  $24^\circ$  are assigned to  $(001)_\gamma$ ,  $(200)_\alpha$ ,  $(020)_\gamma$ ,  $(002)_\alpha$  of crystalline PA6, respectively [50]. No crystalline peaks of  $\text{Fe}(\text{OH})_3$  were observed in XRD, further confirming the  $\text{Fe}(\text{OH})_3$  was amorphous in the nanofibrous scaffold. The results are consistent with the HRTEM and SAED observations. This finding has significant implications for the development of positive contrast  $\text{PA6}/\text{Fe}(\text{OH})_3$  nanofibrous scaffold as the enhanced crystallinity typically correlates with a

higher degree of magnetic spin order within the crystals, thereby yielding an increased  $T_2$  relaxivity [16].

Previously, ligand stabilization methods have been widely employed to enhance metal dispersion and improve the stability of metal sites [43]. Therefore, we have chosen PA6, a polymer with functional groups capable of coordinating with iron, as the fibrous matrix. To investigate the coordination performance between iron and PA6, FTIR characterization was utilized. The characteristic peaks in the FTIR spectrum of pristine PA6 (*i.e.* OPA6 scaffold, Figure S4) showed a sharp peak at  $3300\text{ cm}^{-1}$ , corresponding to the N-H stretching vibrations [51]. The absorption bands at around  $2930\text{ cm}^{-1}$  and  $2850\text{ cm}^{-1}$  were ascribed to the asymmetric and symmetric stretching vibrations of  $-\text{CH}_2$ . The absorption peaks for OPA6 scaffold at around  $1547\text{ cm}^{-1}$  and  $1640\text{ cm}^{-1}$  were assigned to the N-H and C=O stretching vibrations, respectively [52]. Furthermore, the absorption peaks of  $\nu(\text{N-H})$  for 0.1PA6 scaffold were  $1545\text{ cm}^{-1}$  and for 0.2PA6 - 7PA6 scaffolds were around  $1540\text{ cm}^{-1}$  with red shifts observed, revealing that there were significant interactions between N-H and Fe. The C=O absorption band for 0.1PA6 - 2PA6 scaffolds were the same as OPA6 scaffold, which was  $1640\text{ cm}^{-1}$ . However, absorption peaks for 4PA6 scaffold and 7PA6 scaffold were  $1638$  and  $1636\text{ cm}^{-1}$ , respectively. The increased red shift of  $\nu(\text{C=O})$  were commensurate with the increased Fe concentration, indicating enhancing intramolecular coordination [45]. Other research has found that different ligands can vary MRI performance by influencing the water exchange rate [53] and the number of coordinated water molecules [54] of the paramagnetic ions.

TGA was conducted to understand the thermal behavior and stability of  $\text{PA6}/\text{Fe}(\text{OH})_3$  nanofibrous scaffold. All TGA thermograms reveal a weight loss step at temperatures ranging from  $30$  to  $80^\circ\text{C}$  (Figure S5a), which is attributed to the loss of absorbed water vapor on the nanofibrous scaffold because the PA6 nanofibers can readily absorb moisture. The weight loss observed at temperatures ranging from  $320$  to  $500^\circ\text{C}$  was caused by the decomposition of PA6. With an increase in iron content, there was a corresponding increase in the final residual weight, which predominantly consisted of iron-oxygen compounds. Compared to OPA6 scaffold, 0.7PA6 - 7PA6 scaffolds exhibit a subtle weight loss trend from  $80$  to  $320^\circ\text{C}$ . This process is attributed to the dehydration of  $\text{Fe}(\text{OH})_3$ , as indicated by the decrease in weight percentage observed as the Fe-content in nanofibrous scaffolds increases within the range of  $80$  to  $320^\circ\text{C}$ . For instance, 7PA6 scaffold shows a decrease from  $96.6\%$  to  $93.6\%$  while OPA6 scaffold showed no distinct weight loss from  $80$  to  $320^\circ\text{C}$  (Figure S5b). This observation provides further evidence for the presence of iron in the form of  $\text{Fe}(\text{OH})_3$  within the PA6 nanofibers [55].

In order to evaluate the mechanical properties and performance of  $\text{PA6}/\text{Fe}(\text{OH})_3$  nanofibrous scaffold, the mechanical performance of the OPA6 - 7PA6 scaffolds, tensile test were performed (Figure S6a). The incorporation of  $\text{Fe}(\text{OH})_3$  increased the Young's modulus, elongation at break and tensile strength when the iron content was less than  $0.16\text{ wt}\%$ . This is due to the strong coordination between  $\text{Fe}^{3+}$  and N-H and C=O functional groups [56]. However, as the iron concentration increased, grains appeared in the nanofibrous scaffolds and became stress

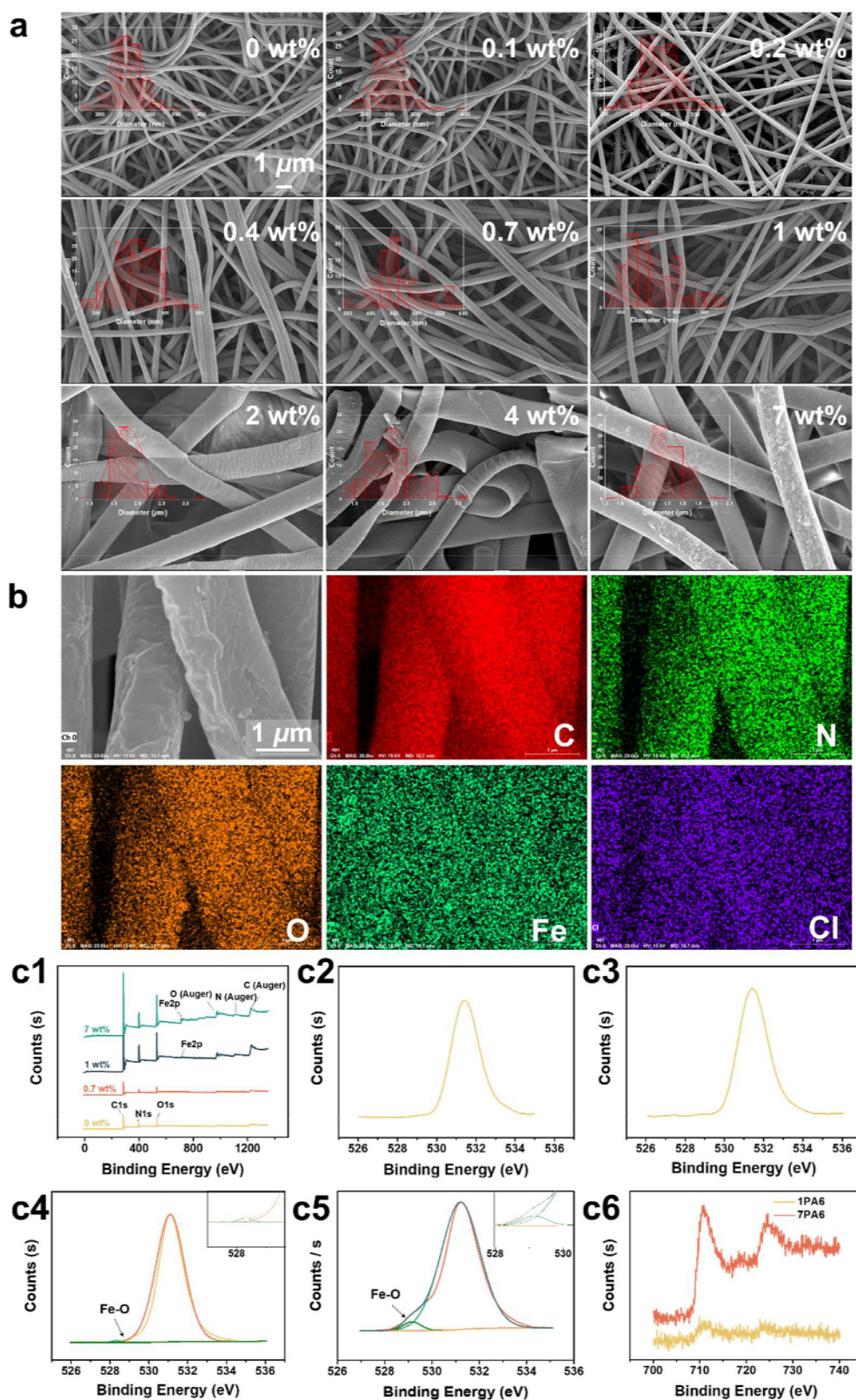
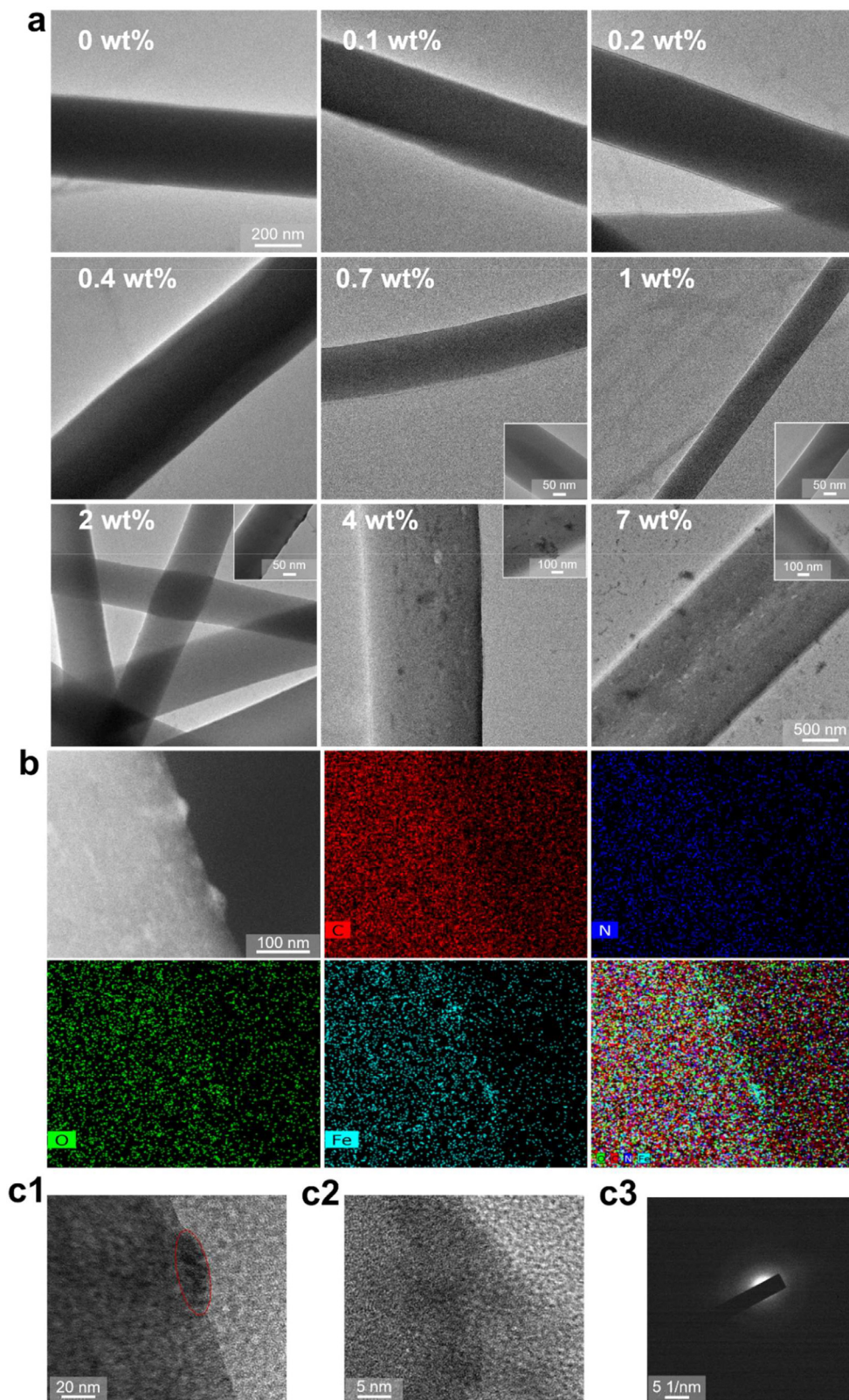


Fig. 2

(a) SEM images of PA6/Fe(OH)<sub>3</sub> nanofibrous scaffold with different iron contents (the white numbers in the pictures denote Fe wt%). The overlaid illustrations depict a histogram of the fiber diameter statistics, with each bar representing the frequency of fibers within a specific diameter range. The data come from over 100 fibers in each sample analyzed by imageJ. All the images have the same scale, as indicated by the scale bar in the first image. (b) SEM mapping analysis of 7PA6 scaffold of the C, N, O, Fe, Cl elements. (c1) XPS full scan spectra of 0PA6, 0.7PA6, 1PA6, 7PA6 scaffolds, O1s scans of (c2) 0 (c3) 0.7 (c4) 1 (c5) 7PA6 scaffolds, and (c6) Fe2p scan of 1PA6 and 7PA6 scaffolds. Insets (in c4 and c5) show the local magnification of the region between 527–530 eV.

**Fig. 3**

(a) TEM images of PA6/Fe(OH)<sub>3</sub> nanofibrous scaffold with different iron contents (the white numbers in the pictures denote Fe wt%, 0PA6 - 4PA6 scaffolds share the same scalebar), The insets in TEM images are magnifications, as indicated by the scale bars. (b) Elemental mapping of Fe(OH)<sub>3</sub> grains on the surface of the 7PA6 scaffold. (c1) HRTEM of Fe(OH)<sub>3</sub> grains. (c2) Corresponding magnified view of the Fe(OH)<sub>3</sub> grains in c1 (highlighted by the red circle). (c3) SAED of the Fe(OH)<sub>3</sub> grains.

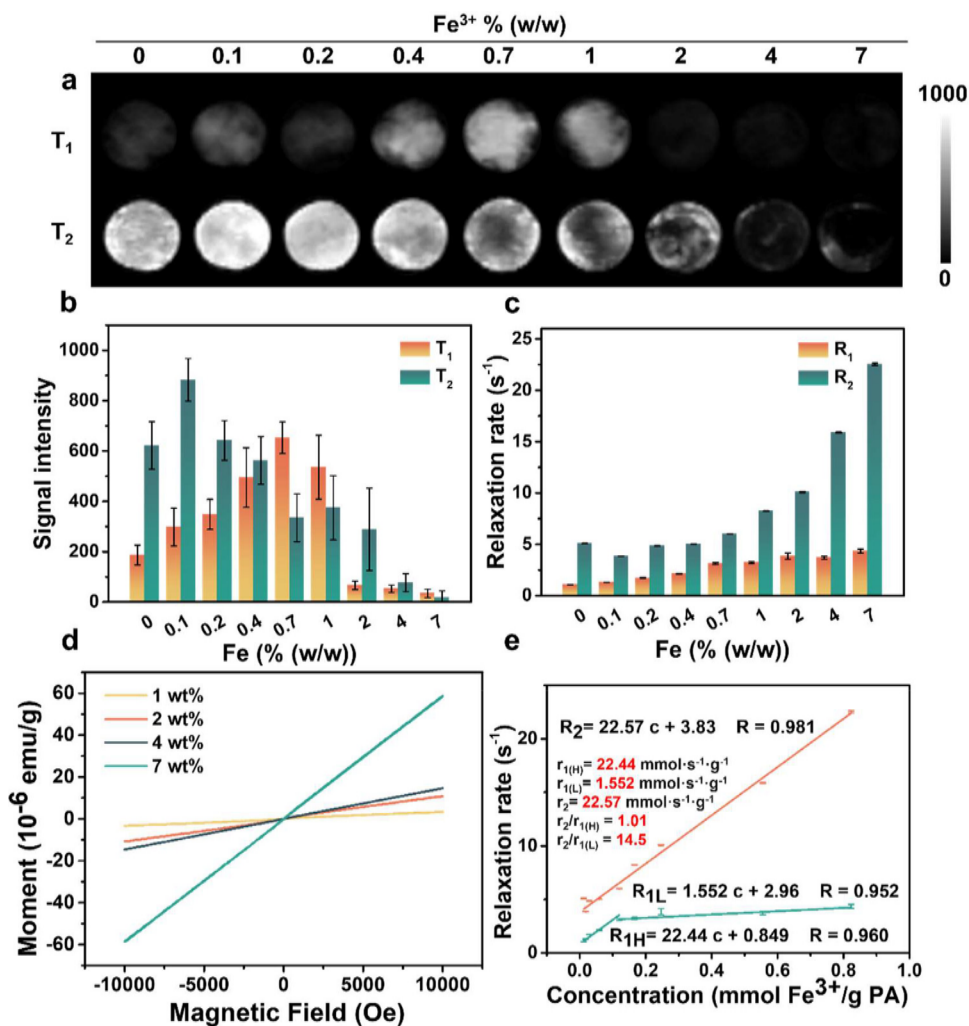


Fig. 4

(a) *In vitro* MRI images of 0PA6 - 7PA6 scaffolds for T<sub>1</sub>WI (top row) and T<sub>2</sub>WI (bottom row). 0.7PA6 scaffold possessed the highest signal in the T<sub>1</sub>WI, the 7PA6 scaffold possessed the lowest signal in the T<sub>2</sub>WI. (b) Signal intensities of T<sub>1</sub> and T<sub>2</sub> for each sample from the corresponding *in vitro* MRI signal images. (c) R<sub>1</sub> and R<sub>2</sub> relaxation rates of each sample measured by LFNMR. (d) Field-dependent magnetization curves (at 298 K, 1T) of 0PA6 - 7PA6 scaffolds. (e) Correlation curves between relaxation rate and iron concentration in nanofibrous scaffolds (linear fit).

concentration points, leading to fracture and thus impairing the mechanical strength.

The future potential of these fibrous systems lies in the field of biomedical applications, making it crucial to assess the release rate of Fe(OH)<sub>3</sub> in simulated bodily fluid environments. We evaluated the iron release performance of the 0.2PA6, 0.7PA6, 2PA6 and 7PA6 scaffolds over a period of 8 days (Figure S6b). The iron released in the PBS (pH = 7.4) solution alone was lower than the detection limit of ICP-OES, as expected. For 0.2PA6 scaffold, the iron release attained a steady state within 5 days with approximately about 20 wt% of the iron released from the nanofibrous scaffold. For 0.7PA6, 2PA6, and 7PA6 scaffolds, the iron release saturated within 5 days and approximately 1-3 wt% of iron was released from the scaffold.

### 3.2 *In vitro* evaluation of magnetic properties of PA6/Fe(OH)<sub>3</sub> nanofibrous scaffold

The hysteresis curves of 1PA6 - 7PA6 scaffolds were measured using PPMS, as shown in Fig. 4d. Hysteresis of the nanofibrous

scaffolds indicates that the nanofibrous scaffolds are paramagnetic [12]. The order of strength of the magnetization at 1T was in the order of 7PA6 > 4PA6 > 2PA6 > 1PA6 scaffold. Generally, for composite systems, the saturation of the magnetization (M<sub>s</sub>) of the composite system is linearly correlated with the content of the magnetic components and the diamagnetic components impair the M<sub>s</sub> value [17]. Here, 0PA6 scaffold itself was nonmagnetic [17] and the M<sub>s</sub> value was impaired, while Fe(OH)<sub>3</sub> increased M<sub>s</sub>. Thus the magnetization of the scaffolds at 1T increased with increasing Fe(OH)<sub>3</sub> content. In addition, it is known that the magnetization strength  $M_2^2 \propto r_2$  [25], and low r<sub>2</sub> values contribute to low r<sub>2</sub>/r<sub>1</sub> values. Therefore, suppressed magnetization could be advantageous for applications of T<sub>1</sub>-weighted candidates.

*In vitro* T<sub>1</sub>WI and T<sub>2</sub>WI were conducted to visualize the labeled scaffolds and quantify the corresponding signal (Fig. 4a, b). In T<sub>1</sub>WI, 0.1PA6 - 1PA6 scaffolds exhibited a positive contrast effect (region of interest being brighter than the 0PA6 scaffold). 0.7PA6 scaffold showed the best signal in T<sub>1</sub>WI. Conversely, 2PA6 - 7PA6

scaffolds exhibit a negative contrast effect (region of interest brighter than the OPA6 scaffold). In  $T_2$  WI, almost all of the materials showed increased darkening with increasing  $\text{Fe}(\text{OH})_3$  concentration.  $R_1$  and  $R_2$  values were calculated by the  $T_1$  and  $T_2$  values measured by LFNMR tests (Fig. 4c). An increase in  $R_1$  and  $R_2$  values was detected with an increase in  $\text{Fe}(\text{OH})_3$  concentration. A high ( $r_{1H} = 22.44 \text{ mmol}\cdot\text{s}^{-1}\cdot\text{g}^{-1}$ ) and low ( $r_{1L} = 1.55 \text{ mmol}\cdot\text{s}^{-1}\cdot\text{g}^{-1}$ ) linear relationship between  $R_1$  and the amount of incorporated iron was observed (Fig. 4e). Similarly, a mono-linear fit was observed for  $R_2$  with a slope of  $22.57 \text{ mmol}\cdot\text{s}^{-1}\cdot\text{g}^{-1}$  for OPA6 - 7PA6 scaffolds. The same linear relationships between the amount of incorporated iron and  $R_2$  relaxation rate were observed for ultrasmall super-paramagnetic iron oxide by Mertens *et al.* [8]. All linear fits had high correlation ( $R^2$  linear correlation coefficients: 0.960 for  $r_{1H}$ , 0.952 for  $r_{1L}$  and 0.981 for  $r_2$ ). There was a significant increasing trend in  $R_2$  when the loading was beyond 1.38 wt% (corresponding to  $\geq 2\text{PA6}$  scaffolds). The absence of an inflection point in the  $r_2$  value of PA6/ $\text{Fe}(\text{OH})_3$  scaffolds can be attributed to the dominant influence of the high magnetic moment and the larger effective radius under the external magnetic field. Conversely, the presence of an inflection point in the  $r_1$  value can be explained by the interplay between highly exposed iron centers on the particle surface and the high surface area to volume ratio [57].

### 3.3 In vitro biosafety and cell colonization and adhesion

Before *in vivo* visualization experiments, the cytocompatibility of the PA6/ $\text{Fe}(\text{OH})_3$  nanofibrous scaffold was evaluated. Cell viability and cell proliferation were quantitatively examined by the CCK-8 assay (Fig. 5b). The negligible bio-toxicity of PA6/ $\text{Fe}(\text{OH})_3$  nanofibrous scaffold can be evidenced by the near-100% cell viability up to 24 h soaking solution of OPA6 - 7PA6 scaffolds after 24 hours of incubation. For HUVEC, the viability was over 85% for OPA6 scaffold, and the viability increased with increasing iron content. For 0.7PA6 - 7PA6 scaffolds, the cell viability was over 140%. When the cell viability exceeds 100%, it typically indicates that the sample has a certain degree of promoting effect on cell proliferation. For NIH/3T3 cells, iron was also found to be favorable for cell proliferation, from 90% for OPA6 scaffold to around 110% for 7PA6 scaffold. Because iron to cells is of central importance for cell growth and survival [58], it is speculated that the increase of cell viability with PA6 scaffold is attributed to the appropriate iron load [59]. These results indicate that PA6/ $\text{Fe}(\text{OH})_3$  nanofibrous scaffold is non-toxic to cells.

Blood compatibility of PA6/ $\text{Fe}(\text{OH})_3$  nanofibrous scaffold was studied by hemolysis evaluation using rabbit red blood cells. As shown in Fig. 5c, the hemolysis percentage of all scaffolds was less than 5%. These results indicated the biocompatibility and safety of the scaffold for *in vivo* applications [60].

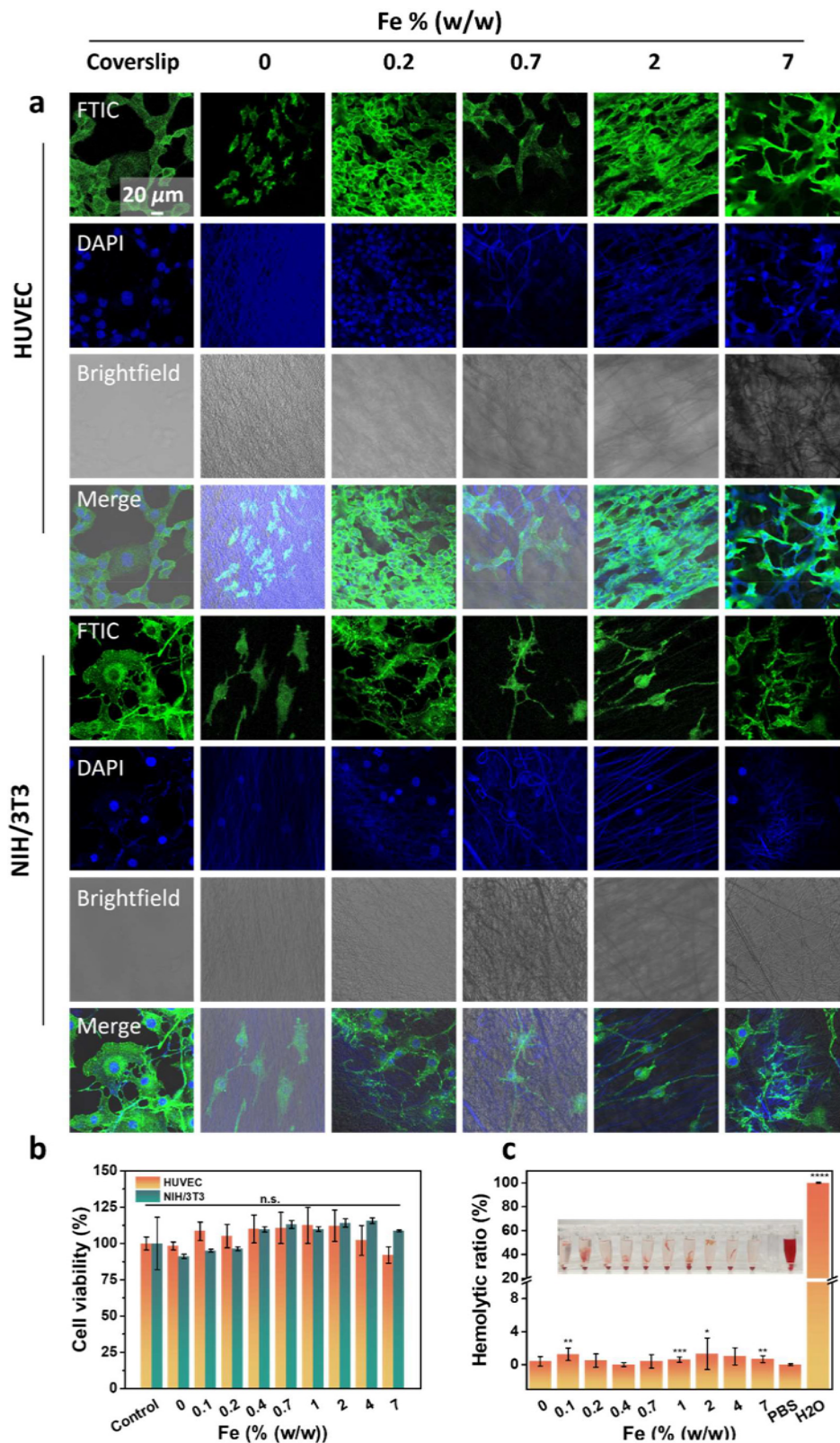
To further evaluate the biocompatibility of PA6/ $\text{Fe}(\text{OH})_3$  nanofibrous scaffold, HUVEC and NIH/3T3 cells were colonized on the nanofibrous scaffolds. CLSM showed that cells in all the groups exhibit excellent adhesion to the scaffolds (Fig. 5a). Compared with the OPA6 scaffold, HUVEC exhibited enhanced spreading on the PA6/ $\text{Fe}(\text{OH})_3$  nanofibrous scaffold. It was also found that  $\text{Fe}(\text{OH})_3$  significantly increased the proliferation of HUVEC, which was consistent with the results of the quantitative

CCK8 assay [61]. In addition, the HUVEC and NIH/3T3 cells cultured on the coverslips and co-incubated with scaffolds exhibited outstanding cellular morphology. The strong affinity of HUVEC and NIH/3T3 cells to the 7PA6 scaffold were more clearly observed by SEM (Figure S7a1, a2) and 3D CLSM images (Figure S7b). These results demonstrate that the PA6/ $\text{Fe}(\text{OH})_3$  nanofibrous scaffold is biocompatible and can allow cell adhesion and proliferation.

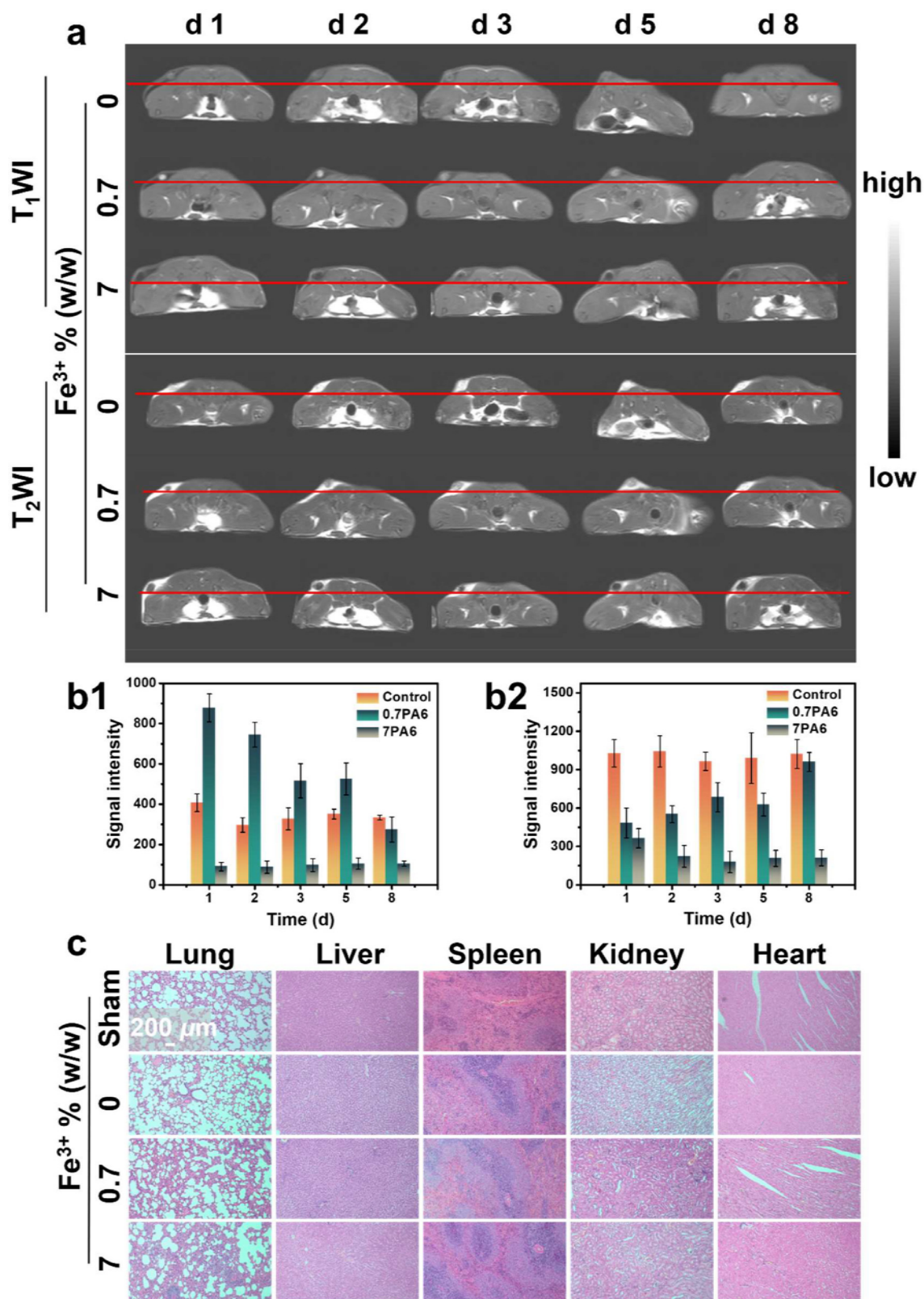
### 3.4 In vivo MRI, biocompatibility and post-implantation morphology

After being washed with deionized water, dried and sterilized using ultraviolet irradiation, the PA6/ $\text{Fe}(\text{OH})_3$  nanofibrous scaffold was subcutaneously implanted into rats as proof for *in vivo* visualization. As an initial proof-of-principle for the *in vivo* visibility and longitudinal monitorability of the scaffold, an unlabeled control, 0.7PA6 scaffold (brightest in  $T_1$ WI image *in vitro*) and 7PA6 scaffold (darkest in  $T_2$ WI image *in vitro*) were subcutaneously implanted on the left side of SD female rats. As shown in Figure 6a, animals were longitudinally monitored for 8 days via MRI. The absolute signal intensity of 0.7PA6 scaffold was much higher (880) than the unlabeled control (400) in  $T_1$ WI on day 1 following implantation (Figure 6b1). The  $T_1$ WI signal of 0.7PA6 scaffold gradually decayed with time. On day 8 (since implantation), the positive contrast effect had gradually decayed and was similar to OPA6 scaffold. However, for 7PA6 scaffold, the signals maintained a low value (around 100) in  $T_1$ WI. In the  $T_2$ -weighted images, the signal values of the 0.7PA6 scaffold and 7PA6 scaffold were both lower than the control group (Fig. 6b2). Notably, on day 1, the signal value of 0.7PA6 scaffold was approximately 500 lower than the control group, and the signal value of 7PA6 scaffold was approximately 650, lower than that of the control group. On day 8 following implantation, the signal intensity of the 0.7PA6 scaffold approached a value close to that of the control due to the release of iron, while the signal intensity of the 7PA6 scaffold remained stable at a low level (around 200). We speculate that the slightly higher signal value of the 7PA6 scaffold group on the 1<sup>st</sup> day after implantation compared to days 2 - 8 was due to postoperative edema.

The implants were removed from the subcutaneous area of the rats at 1, 3 and 8 days after implantation, and the implant morphology was observed by SEM after gradient ethanol dehydration. *Ex vivo* SEM and EDS mapping (Figure S8a) showed that all fibers retained their fibrous morphology after 8 days of implantation; wrinkles appeared on the surface of the fibers but no signs of fiber degradation, indicating the decay of the signals were not caused by the degradation of the scaffold. However, ICP-OES indicated that the iron content in the 0.7PA6 scaffold decreased from 0.67 wt% before implantation to 0.057 wt% after 8 days since implantation, evidencing the signal decay of 0.7PA6 scaffold was due to the release of iron. The 7PA6 scaffold surface was covered by granules and membrane-like material, presumably extracellular proteins. 0.7PA6 scaffold had almost complete loss of iron in the fibers after 8 days, while some granules were observed on the surface of 7PA6 scaffold after 8 days (Figure S8b), and the EDS results indicated that these granules were high in iron content and were similar to those grains observed before implantation.

**Fig. 5**

(a) *In vitro* HUVEC and NIH/3T3 cell attachment on the 0PA6, 0.2PA6, 0.7 PA6, 2PA6, and 7PA6 scaffolds, with a coverslip used as a control group. Each scaffold was seeded with approximately 50k cells and cultured for 48h [FITC-stained cytoskeleton (green), DAPI-stained nucleus (blue)]. (All images share a common scale). (b) CCK8 assay of HUVEC treated with soaking solution of 0PA6 - 7PA6 scaffolds. The data are shown as a mean  $\pm$  standard deviation ( $n = 3 - 6$ ). (c) Photos and quantitative assays of hemolysis of 0PA6 - 7PA6 scaffolds. The presence of red blood cells in the middle and upper regions of the centrifuge tube in the photograph is attributed to the strong adsorption capacity of PA6 nanofibers towards red blood cells. The data are shown as a mean  $\pm$  standard deviation ( $n = 6$ ). The groups without asterisks were considered non-significant (n.s.).

**Fig. 6**

*In vivo* monitoring of PA6/Fe(OH)<sub>3</sub> nanofibrous scaffold. (a) T<sub>1</sub>WI and T<sub>2</sub>WI of subcutaneously implanted PA6/Fe(OH)<sub>3</sub> nanofibrous scaffold for 8 days. The red lines indicate the location of implanted samples in each mouse. (b1,b2) Comparison of the T<sub>1</sub>WI and T<sub>2</sub>WI absolute signal intensity of PA6/Fe(OH)<sub>3</sub> nanofibrous scaffold and unlabeled controls during the monitoring period. (c) H&E staining of the lung, liver, spleen, kidney, heart tissues from the mice after 8 days of implantation (All images share a common scale.).

The presence of the Fe(OH)<sub>3</sub> grains could be the reason why the 7PA6 scaffold maintained a better negative contrast signal after 8 days.

Major organs of the sham group and all experimental groups of SD rats were harvested on day 8 and evaluated by H&E staining (Fig. 6c). From the H&E staining images, the OPA6, 0.7PA6, 7PA6 scaffolds implantation groups showed no obvious distinction from the sham group and no toxicity or major organ degenerative changes were observed. The obtained results provide confirmation of the excellent biocompatibility of PA6/Fe(OH)<sub>3</sub> nanofibrous scaffold and lend support to their potential for clinical applications.

## 4 Conclusions

Iron-based PA6 nanofibrous tissue engineering scaffolds have been fabricated with a positive MRI contrast effect. MRI visualization was performed for geometric evaluation of the complex shape of the scaffolds. The results of cellular experiments showed that the scaffold greatly promoted the proliferation of endothelial cells and fibroblasts, with an increase in iron concentration in the scaffold leading to the transition from positive to negative MRI contrast. Results of *in vivo* experiments showed that the positive contrast scaffold maintained good signal intensity for the first 5 days before the signal eventually decayed over the following 3 days. All stents showed no significant degradation after 8 days in addition to no significant damage to major organs. The scaffold holds potential for early disease diagnosis, providing high contrast imaging signals during that timeframe. It can aid in the early detection of disease signs or abnormalities, allowing for timely therapeutic interventions. Additionally, this scaffold can be custom-designed with biological activity, targeting specificity, and thus meeting the needs of different tissue engineering fields. Overall, this novel scaffold possesses significant potential for future investigations of biomaterial response *in vivo* and creation of non-invasive, clinically oriented monitoring systems for tissue engineering scaffolds.

## Declaration of competing interest

The authors declare that they have no known competing financial interests or personal relationships that could have appeared to influence the work reported in this paper.

## Data availability

Data will be made available on request.

## CRediT authorship contribution statement

**Congyi Yang:** Writing – review & editing, Writing – original draft, Methodology, Formal analysis, Data curation. **Yifan Jia:** Validation, Methodology, Investigation, Formal analysis. **Weiwen Yuan:** Validation, Formal analysis. **Guoxing Liao:** Writing – review & editing. **Qianqian Yu:** Writing – review & editing, Methodology, Funding acquisition, Formal analysis, Data curation. **Zhe Tang:** Methodology, Formal analysis. **Yuan Ji:** Validation. **Guanghui Liu:** Validation. **Fangrong Tan:** Validation. **Paul D. Topham:** Writing – review & editing, Data curation. **LinGe Wang:** Writing – review & editing, Writing

– original draft, Supervision, Resources, Methodology, Funding acquisition, Data curation, Conceptualization.

## Acknowledgment

The authors thank the financial support from the National Natural Science Foundation of China (No. U22A20316), Science and Technology Program of Guangzhou (No. 2023B03J0037), Overseas Expertise Introduction Center for Discipline Innovation (“111 Center”) and the Fundamental Research Funds for the Central Universities (No. 2023ZYGXZR051).

## Supplementary materials

Supplementary material associated with this article can be found, in the online version, at doi:10.1016/j.giant.2024.100259.

## References

- [1] A.K. Gaharwar, I. Singh, A. Khademhosseini, Engineered biomaterials for in situ tissue regeneration, *Nat. Rev. Mater.* 5 (2020) 686–705, doi:10.1038/s41578-020-0209-x.
- [2] Z. Chen, W. Zhang, M. Wang, L.J. Backman, J. Chen, Effects of zinc, magnesium, and iron ions on bone tissue engineering, *ACS Biomater. Sci.* 8 (2022) 2321–2335, doi:10.1021/acsbomaterials.2c00368.
- [3] J. Li, N. Zhuo, J. Zhang, Q. Sun, J. Si, K. Wang, D. Zhi, The loading of C-type natriuretic peptides improved hemocompatibility and vascular regeneration of electrospun poly( $\epsilon$ -caprolactone) grafts, *Acta Biomater.* 151 (2022) 304–316, doi:10.1016/j.actbio.2022.08.032.
- [4] Y. Zhao, Y. Liang, S. Ding, K. Zhang, H. Mao, Y. Yang, Application of conductive PPy/SF composite scaffold and electrical stimulation for neural tissue engineering, *Biomaterials* 255 (2020) 120164, doi:10.1016/j.biomaterials.2020.120164.
- [5] S. Zhang, G. Zhao, W. Ma, Y. Song, C. Huang, C. Xie, K. Chen, X. Li, The root-like chitosan nanofiber porous scaffold cross-linked by genipin with type I collagen and its osteoblast compatibility, *Carbohydr. Polym.* 285 (2022) 119255, doi:10.1016/j.carbpol.2022.119255.
- [6] M. Licciardello, C.Tonda Turo, A. Gallina, G. Ciofani, G. Ciardelli, Fabrication of extracellular matrix-like membranes for loading piezoelectric nanoparticles, *J. Phys. Mater.* 3 (2020) 034004, doi:10.1088/2515-7639/ab8572.
- [7] Z. Li, D. Chu, Y. Gao, L. Jin, X. Zhang, W. Cui, J. Li, Biomimicry, biomineralization, and bioregeneration of bone using advanced three-dimensional fibrous hydroxyapatite scaffold, *Mater. Today Adv.* 3 (2019) 10014, doi:10.1016/j.mtadv.2019.100014.
- [8] M.E. Mertens, A. Hermann, A. Buehren, L. Olde Damink, D. Moeckel, F. Gremse, J. Ehling, F. Kiessling, T. Lammers, Iron oxide-labeled collagen scaffolds for non-invasive MR imaging in tissue engineering, *Adv. Funct. Mater.* 24 (2014) 754–762, doi:10.1002/adfm.201301275.
- [9] Y. Yang, S.M. Dorsey, M.L. Becker, S. Lin Gibson, G.E. Schumacher, G.A. Flaim, J. Kohn, C.G. Simon Jr., X-ray imaging optimization of 3D tissue engineering scaffolds via combinatorial fabrication methods, *Biomaterials* 29 (2008) 1901–1911, doi:10.1016/j.biomaterials.2007.12.042.
- [10] Y.K. Fan, S.M. Feng, X.L. Liu, K.Q. Li, D.L. Chen, C.D. Xiong, Synthesis and characterization of novel radiopaque polycarbonate, *Macromol. Rapid Commun.* 43 (2022) 2100906, doi:10.1002/marc.202100906.
- [11] N. Celikkin, S. Mastrogiacomo, X.F. Walboomers, W. Swieszkowski, Enhancing X-ray attenuation of 3D printed gelatin methacrylate (GelMA) hydrogels utilizing gold nanoparticles for bone tissue engineering applications, *Polymers* 11 (2019) 367, doi:10.3390/polym11020367.
- [12] Y. Jia, W. Yuan, M. Xu, C. Yang, L. Chen, S. Wang, P.D. Topham, G. Luo, M. Wang, Y. Zhang, G. Jiang, Q. Yu, L. Wang, One-step method to fabricate poly(ethylene terephthalate)/Gd(OH)<sub>3</sub> magnetic nanofibers towards MRI-active materials with high T<sub>1</sub> relaxivity and long-term visibility, *Giant* 12 (2022) 100121, doi:10.1016/j.giant.2022.100121.
- [13] Y. Du, Y. Huo, Q. Yang, Z. Han, L. Hou, B. Cui, K. Fan, Y. Qiu, Z. Chen, W. Huang, J. Lu, L. Cheng, W. Cai, L. Kang, Ultrasmall iron-gallic acid coordination polymer nanodots with antioxidative neuroprotection for PET/MR imaging-guided ischemia stroke therapy, *Exploration* 3 (2023) 20220041, doi:10.1002/EXP.20220041.
- [14] K. Kim, C.G. Jeong, S.J. Hollister, Non-invasive monitoring of tissue scaffold degradation using ultrasound elasticity imaging, *Acta Biomater.* 4 (2008) 783–790, doi:10.1016/j.actbio.2008.02.010.
- [15] S. Mastrogiacomo, W. Dou, J.A. Jansen, X.F. Walboomers, Magnetic resonance imaging of hard tissues and hard tissue engineered bio-substitutes, *Mol. Imaging Biol.* 21 (2019) 1003–1019, doi:10.1007/s11307-019-01345-2.
- [16] Z. Zhou, L. Yang, J. Gao, X. Chen, Structure-relaxivity relationships of magnetic nanoparticles for magnetic resonance imaging, *Adv. Mater.* 31 (2019) e1804567, doi:10.1002/adma.201804567.

- [17] Y.F. Jia, C.Y. Yang, X.Y. Chen, W.Q. Xue, H.J. Hutchins Crawford, Q.Q. Yu, P.D. Topham, L.G. Wang, A review on electrospun magnetic nanomaterials: methods and applications, *J. Mater. Chem. C* 9 (2021) 9042–9082, doi:10.1039/d1tc01477c.
- [18] H. Perea, J. Aigner, J.T. Heverhagen, U. Hopfner, E. Wintermantel, Vascular tissue engineering with magnetic nanomaterials: seeing deeper, *J. Tissue Eng. Regen. Med.* 1 (2007) 318–321, doi:10.1002/term.32.
- [19] C. Constantinides, P. Basnett, B. Lukasiewicz, R. Carnicer, E. Swider, Q.A. Majid, M. Srinivas, C.A. Carr, I. Roy, In vivo tracking and  $^1\text{H}/^{19}\text{F}$  magnetic resonance imaging of biodegradable polyhydroxyalkanoate/polycaprolactone blend scaffolds seeded with labeled cardiac stem cells, *ACS Appl. Mater.* 10 (2018) 25056–25068, doi:10.1021/acsami.8b06096.
- [20] M.E. Mertens, S. Koch, P. Schuster, J. Wehner, Z. Wu, F. Gremse, V. Schulz, L. Rongen, F. Wolf, J. Frese, V.N. Gesché, M. van Zandvoort, P. Mela, S. Jockenhoevel, F. Kiessling, T. Lammers, USPIO-labeled textile materials for non-invasive MR imaging of tissue-engineered vascular grafts, *Biomaterials* 39 (2015) 155–163, doi:10.1016/j.biomaterials.2014.10.076.
- [21] N.E. Putra, M.A. Leeftang, M. Klimopoulou, J. Dong, P. Taheri, Z. Huan, L.E. Fratila Apachitei, J.M.C. Mol, J. Chang, J. Zhou, A.A. Zadpoor, Extrusion-based 3D printing of biodegradable, osteogenic, paramagnetic, and porous FeMn-akermanite bone substitutes, *Acta Biomater.* 162 (2023) 182–198, doi:10.1016/j.actbio.2023.03.033.
- [22] S. Leon Chaviano, M. Kiseleva, P. Legros, S. Collin, T. Lescot, C. Henoumont, Y. Gossuin, S. Laurent, D. Mayrand, J. Fradette, A. Bégin Drolet, J. Ruel, M.A. Fortin, A nanoparticle ink allowing the high precision visualization of tissue engineered scaffolds by MRI, *Small* 19 (2023) 2206644, doi:10.1002/smll.202206644.
- [23] F.H.L. Starsich, C. Eberhardt, K. Keevend, A. Boss, A.M. Hirt, I.K. Herrmann, S.E. Pratsinis, Reduced magnetic coupling in ultrasmall iron oxide  $\text{T}_1$  MRI contrast agents, *ACS Appl. Bio Mater.* 1 (2018) 783–791, doi:10.1021/acsabm.8b00244.
- [24] O.U. Akakuru, M.Z. Iqbal, M. Saeed, C. Liu, T. Paunesku, G. Woloschak, N.S. Hosmane, A. Wu, The transition from metal-based to metal-free contrast agents for  $\text{T}_1$  magnetic resonance imaging enhancement, *Bioconjugate Chem* 30 (2019) 2264–2286, doi:10.1021/acs.bioconjchem.9b00499.
- [25] Y.K. Peng, C.L. Liu, H.C. Chen, S.W. Chou, W.H. Tseng, Y.J. Tseng, C.C. Kang, J.K. Hsiao, P.T. Chou, Antiferromagnetic iron nanocolloids: a new generation in vivo  $\text{T}_1$  MRI contrast agent, *J. Am. Chem. Soc.* 135 (2013) 18621–18628, doi:10.1021/ja409490q.
- [26] D. Liu, J. Li, C. Wang, L. An, J. Lin, Q. Tian, S. Yang, Ultrasmall  $\text{Fe}@\text{Fe}_3\text{O}_4$  nanoparticles as  $\text{T}_1$ - $\text{T}_2$  dual-mode MRI contrast agents for targeted tumor imaging, *Nanomed. Nanotechnol.* 32 (2021) 102335, doi:10.1016/j.nano.2020.102335.
- [27] M. Ma, H. Zhu, J. Ling, S. Gong, Y. Zhang, Y. Xia, Z. Tang, Quasi-amorphous and hierarchical  $\text{Fe}_2\text{O}_3$  supraparticles: active  $\text{T}_1$ -weighted magnetic resonance imaging in vivo and renal clearance, *ACS Nano* 14 (2020) 4036–4044, doi:10.1021/acsnano.9b08570.
- [28] Y. Bao, J.A. Sherwood, Z. Sun, Magnetic iron oxide nanoparticles as  $\text{T}_1$  contrast agents for magnetic resonance imaging, *J. Mater. Chem. C* 6 (2018) 1280–1290, doi:10.1039/C7TC05854C.
- [29] L. Zeng, W. Ren, J. Zheng, A. Wu, P. Cui, Synthesis of water-soluble  $\text{Fe}(\text{OH})$  nanospindles and their performance for magnetic resonance imaging, *Appl. Surf. Sci.* 258 (2012) 2570–2575, doi:10.1016/j.apsusc.2011.10.093.
- [30] T. Macher, J. Totenhagen, J. Sherwood, Y. Qin, D. Gurler, M.S. Bolding, Y. Bao, Ultrathin iron oxide nanowhiskers as positive contrast agents for magnetic resonance imaging, *Adv. Funct. Mater.* 25 (2015) 490–494, doi:10.1002/adfm.201403436.
- [31] H. Awada, S. Sene, D. Laurencin, L. Lemaire, F. Franconi, F. Bernex, A. Bethry, X. Garric, Y. Guari, B. Nottelet, Long-term in vivo performances of poly(lactide)/iron oxide nanoparticles core-shell fibrous nanocomposites as MRI-visible magneto-scaffolds, *Biomater. Sci.* 9 (2021) 6203–6213, doi:10.1039/d1bm00186h.
- [32] E. Rama, S.R. Mohapatra, C. Melcher, T. Nolte, S.M. Dadfar, R. Brueck, V. Pathak, A. Rix, T. Gries, V. Schulz, T. Lammers, C. Apel, S. Jockenhoevel, F. Kiessling, Monitoring the remodeling of biohybrid tissue-engineered vascular grafts by multimodal molecular imaging, *Adv. Sci.* 9 (2022) 2105783, doi:10.1002/adv.202105783.
- [33] L. Wang, M. Wang, P.D. Topham, Y. Huang, Fabrication of magnetic drug-loaded polymeric composite nanofibers and their drug release characteristics, *RSC Adv* 2 (2012) 2433–2438, doi:10.1039/C2RA00484D.
- [34] D. Ray, S. Sain, In situ processing of cellulose nanocomposites, *Compos. Part A-Appl. Sci.* 83 (2016) 19–37, doi:10.1016/j.compositesa.2015.09.007.
- [35] Y. Feng, M. Zhang, Y. Sun, C. Cao, J. Wang, M. Ge, W. Cai, J. Mi, Y. Lai, Porous carbon nanofibers supported  $\text{Zn}@\text{MnO}_x$  sorbents with high dispersion and loading content for hot coal gas desulfurization, *Chem. Eng. J.* 464 (2023) 142590, doi:10.1016/j.cej.2023.142590.
- [36] Z.M. Huang, Y.Z. Zhang, M. Kotaki, S. Ramakrishna, A review on polymer nanofibers by electrospinning and their applications in nanocomposites, *Compos. Sci. Technol.* 63 (2003) 2223–2253, doi:10.1016/S0266-3538(03)00178-7.
- [37] B. Ding, M.R. Wang, X.F. Wang, J.Y. Yu, G. Sun, Electrospun nanomaterials for ultrasensitive sensors, *Mater. Today* 13 (2010) 16–27, doi:10.1016/S1369-7021(10)70200-5.
- [38] D. Kai, G. Jin, M.P. Prabhakaran, S. Ramakrishna, Electrospun synthetic and natural nanofibers for regenerative medicine and stem cells, *Biotechnol. J.* 8 (2013) 59–72, doi:10.1002/biot.201200249.
- [39] J.J. Xue, J.W. Xie, W.Y. Liu, Y.N. Xia, Electrospun nanofibers: new concepts, materials, and applications, *Acc. Chem. Res.* 50 (2017) 1976–1987, doi:10.1021/acs.accounts.7b00218.
- [40] L. Chen, S. Wang, Q. Yu, P.D. Topham, C. Chen, L. Wang, A comprehensive review of electrospinning block copolymers, *Soft Matter* 15 (2019) 2490–2510, doi:10.1039/c8sm02484g.
- [41] J.J. Xue, T. Wu, Y.Q. Dai, Y.N. Xia, Electrospinning and electrospun nanofibers: methods, materials, and applications, *Chem. Rev.* 119 (2019) 5298–5415, doi:10.1021/acs.chemrev.8b00593.
- [42] L. Chen, Q. Yu, Y. Jia, M. Xu, Y. Wang, J. Wang, T. Wen, L. Wang, Micro-and-nanometer topological gradient of block copolymer fibrous scaffolds towards region-specific cell regulation, *J. Colloid Interf. Sci.* 606 (2022) 248–260, doi:10.1016/j.jcis.2021.08.021.
- [43] Y. Yang, X. Liu, Y. Lyu, Y. Liu, W. Zhan, Z. Yu, L. Fan, Z. Yan, Enhanced dispersion of nickel nanoparticles on SAPO-5 for boosting hydroisomerization of n-hexane, *J. Colloid Interf. Sci.* 604 (2021) 727–736, doi:10.1016/j.jcis.2021.07.039.
- [44] M. Shakiba, E. Rezvani Ghomi, F. Khosravi, S. Jouybar, A. Bigham, M. Zare, M. Abdouss, R. Moaref, S. Ramakrishna, Nylon-A material introduction and overview for biomedical applications, *Polym. Advan. Technol.* 32 (2021) 3368–3383, doi:10.1002/pat.5372.
- [45] J. Liu, R. Wu, R. Gu, F. Qiu, J. Pan, Simple formation of chitosan tablet with self-supporting blocks:  $\text{Fe}^{3+}$  mediated supramolecular coordination, *Chem. Eng. J.* 341 (2018) 648–657, doi:10.1016/j.cej.2018.02.008.
- [46] F.J. Bye, L. Wang, A.J. Bullock, K.A. Blackwood, A.J. Ryan, S. MacNeil, Postproduction processing of electrospun fibres for tissue engineering, *J. Vis. Exp.* 9 (2012) e4172, doi:10.3791/4172.
- [47] D. Shan, Y. Shi, S. Duan, Y. Wei, Q. Cai, X. Yang, Electrospun magnetic poly(L-lactide) (PLLA) nanofibers by incorporating PLLA-stabilized  $\text{Fe}_3\text{O}_4$  nanoparticles, *Mat. Sci. Eng. C-Mater.* 33 (2013) 3498–3505, doi:10.1016/j.msec.2013.04.040.
- [48] X. Hu, X. Hao, Y. Wu, J. Zhang, X. Zhang, P.C. Wang, G. Zou, X.-J. Liang, Multifunctional hybrid silica nanoparticles for controlled doxorubicin loading and release with thermal and pH dual response, *J. Mater. Chem. B* 1 (2013) 1109–1118, doi:10.1039/c2tb00223j.
- [49] D. Zhang, F. Peng, J. Tan, Y. Zhang, F. Wang, J. Xie, R. Xu, H. Du, S. Qian, Y. Qiao, M. Li, X. Liu, Self-assembled ferric oxyhydroxide nanosheet on PEO-coated magnesium alloy with photocatalytic/photothermal antibacterial and enhanced osteogenesis activities, *Chem. Eng. J.* 437 (2022) 135257, doi:10.1016/j.cej.2022.135257.
- [50] Y. Liu, L. Cui, F. Guan, Y. Gao, N.E. Hedin, L. Zhu, H. Fong, Crystalline morphology and polymorphic phase transitions in electrospun nylon-6 nanofibers, *Macromolecules* 40 (2007) 6283–6290, doi:10.1021/ma070039p.
- [51] B.K. Shrestha, H.M. Mousa, A.P. Tiwari, S.W. Ko, C.H. Park, C.S. Kim, Development of polyamide-6,6/chitosan electrospun hybrid nanofibrous scaffolds for tissue engineering application, *Carbohydr. Polym.* 148 (2016) 107–114, doi:10.1016/j.carbpol.2016.03.094.
- [52] H. Zhang, L. Zhang, Q. Jia, C. Shi, J. Yang, Preparation of porous nylon 6 fiber via electrospinning, *Polym. Eng. Sci.* 55 (2015) 1133–1141, doi:10.1002/pen.23984.
- [53] S. Laus, R. Ruloff, É. Tóth, A.E. Merbach, GdIII complexes with fast water exchange and high thermodynamic stability: potential building blocks for high-relaxivity MRI contrast agents, *Chem. Eur. J.* 9 (2003) 3555–3566, doi:10.1002/chem.200204612.
- [54] V.C. Pierre, M. Melchior, D.M.J. Doble, K.N. Raymond, Toward optimized high-relaxivity MRI agents: thermodynamic selectivity of hydroxypyridonate/catecholate ligands, *Inorg. Chem.* 43 (2004) 8520–8525, doi:10.1021/ic0493447.
- [55] X. Zhao, Y. Su, S. Li, Y. Bi, X. Han, A green method to synthesize flowerlike  $\text{Fe}(\text{OH})_3$  microspheres for enhanced adsorption performance toward organic and heavy metal pollutants, *J. Environ. Sci.* 73 (2018) 47–57, doi:10.1016/j.jes.2018.01.010.
- [56] C. Jiao, J. Zhang, T. Liu, X. Peng, H. Wang, Mechanically strong, tough, and shape deformable poly(acrylamide-co-vinylimidazole) hydrogels based on  $\text{Cu}^{2+}$  complexation, *ACS Appl. Mater.* 12 (2020) 44205–44214, doi:10.1021/acsami.0c13654.
- [57] Z. Zhou, Z. Zhao, H. Zhang, Z. Wang, X. Chen, R. Wang, Z. Chen, J. Gao, Interplay between longitudinal and transverse contrasts in  $\text{Fe}_3\text{O}_4$  nanoplates with (111) exposed surfaces, *ACS Nano* 8 (2014) 7976–7985, doi:10.1021/nn5038652.
- [58] J. Zhang, H.S. Shi, J.Q. Liu, T. Yu, Z.H. Shen, J.D. Ye, Good hydration and cell-biological performances of superparamagnetic calcium phosphate cement with concentration-dependent osteogenesis and angiogenesis induced by ferric iron, *J. Mater. Chem. B* 3 (2015) 8782–8795, doi:10.1039/c5tb01440a.

- [59] Z. Tang, M. Zhao, Y. Wang, W. Zhang, M. Zhang, H. Xiao, L. Huang, L. Chen, X. Ouyang, H. Zeng, H. Wu, Mussel-inspired cellulose-based adhesive with biocompatibility and strong mechanical strength via metal coordination, *Int. J. Biol. Macromol.* 144 (2020) 127–134, doi:[10.1016/j.ijbiomac.2019.12.076](https://doi.org/10.1016/j.ijbiomac.2019.12.076).
- [60] Y. Lin, Y. Wan, X. Du, J. Li, J. Wei, T. Li, C. Li, Z. Liu, M. Zhou, Z. Zhong, TAT-modified serum albumin nanoparticles for sustained-release of tetramethylpyrazine and improved targeting to spinal cord injury, *J. Nanobiotechnol.* 19 (2021) 28, doi:[10.1186/s12951-020-00766-4](https://doi.org/10.1186/s12951-020-00766-4).
- [61] W. Ma, X. Zhang, Y. Liu, L. Fan, J. Gan, W. Liu, Y. Zhao, L. Sun, Polydopamine decorated microneedles with Fe-MSC-derived nanovesicles encapsulation for wound healing, *Adv. Sci.* 9 (2022) e2103317, doi:[10.1002/advs.202103317](https://doi.org/10.1002/advs.202103317).